Gravitational lensing and tunneling of mechanical waves in synthetic curved spacetime

Sayan Jana [*] and Lea Sirota [†]
School of Mechanical Engineering, Tel Aviv University, Tel Aviv 69978, Israel

(Received 10 November 2022; accepted 9 July 2023; published 15 August 2023)

Black holes are considered among the most fascinating objects that exist in our universe since in the classical formalism nothing, not even light, can escape from their vicinity due to gravity. The gravitational potential causes the light to bend toward the hole, which is known as gravitational lensing. Here, we present a synthetic realization of this phenomenon in a laboratory-scale two-dimensional network of mechanical circuits, based on analogous condensed matter formalism of Weyl semimetals with inhomogeneous nodal tilt profiles. Some of the underlying network couplings turn out as unstable and nonreciprocal and are implemented by embedded active feedback interactions in an overall stabilized structure. We demonstrate the lensing by propagating mechanical wave packets through the network with a programed funnel-like potential, achieving wave bending toward the circle center. We then demonstrate the versatility of our platform by reprogramming it to mimic quantum tunneling of particles through the event horizon, known as Hawking radiation, achieving an exceptional correspondence to the original mass loss rate within the hole. The network couplings and the potential can be further reprogrammed to realize other curvatures and associated relativistic phenomena.

DOI: 10.1103/PhysRevResearch.5.033104

I. INTRODUCTION

In our universe, the existence of black holes [1] is theoretically predicted by Einstein's theory of general relativity through the spacetime singularity in the Schwarzschild metric [2]. This metric determines the curvature of spacetime geometry for which gravity is the outcome. In classical gravity, the event horizon is thought of as a boundary between the black hole and the visible universe. Any object that crosses this boundary is dragged at the speed of light toward the center and ultimately becomes invisible. The resulting propagation of relativistic light in the curved spacetime around the hole is characterized by deflection or lensing inward due to the gravitational potential.

Recently, a condensed matter analogue of the spacetime curvature has been obtained through Weyl semimetals (WSMs) that are characterized by the Hamiltonian $H_{\mathrm{WSM}} = (V_t + v_f\sigma)\cdot\mathbf{k}$ with a spatially varying tilt profile $V_t(r)$ [3–8]. Here, r and $\mathbf{k}$ are, respectively, the spatial coordinate and the momentum in three dimensions, spanned by Pauli matrices σ. The analogue was drawn pictorially by mapping Weyl cones into spacetime geodesics (light cones), obtained from the Painlevé [9], Gullstrand [10], Lemaître [11] coordinate system:

$$ds^2 = c^2dt^2 - [dr - V(r)dt]^2, \tag{1}$$

in which the spatial profile $V(r)$ incorporates the gravity information, and the event horizon is denoted by the radius where $V(r)$ equals the speed of light c. In the WSM equivalence, the tilt $V_t(r)$ and Fermi velocity v_f are respectively mapped to $V(r)$ and c in Eq. (1), yielding the horizon along r that satisfies $V_t(r) = v_f$. The resulting system can be represented by the quantum Bloch Hamiltonian [12,13]:

$$H(k) = \sum_{j=x,y} t_j(\sigma_j - V_j\sigma_0)\sin k_j a + t_z\sigma_z(2 - \cos k_x a - \cos k_y a), \tag{2}$$

where t_x, t_y indicate the spin-orbit coupling strength, t_z is the nearest-neighbor hopping parameter, V_x, V_y are the x, y projections of the tilting potential $V_t(r)$, and a is the lattice constant. This mapping between two entirely different fields, relativistic physics and quantum condensed matter, is also valid for other high-energy phenomena, such as Klein tunneling in graphene [14], transport in solids, and chiral anomaly in WSM [15]. However, laboratory imitation of high-energy effects, even via the condensed matter analogy [16,17], is not immediate. Here, we present a framework for constructing an experimentally ready purely classical model, consisting of a network of active mechanical circuits [18–23], which realizes, based on the WSM formalism, a synthetic curved spacetime and the associated gravitational lensing. In addition, our platform realizes another aspect of the black hole, which is Hawking radiation, also known as horizon tunneling. The latter stems from the astonishing discovery that, in the quantum realm, the phenomenon of completely black is not entirely true.

Rather, it was shown that a black hole radiates [24–26], and this radiation exists as fluctuation of quantum fields near the horizon with temperature T_H, famously known as the Hawking temperature. Equivalently, Hawking radiation can

[*] sayanjana@tauex.tau.ac.il
[†] leabeilkin@tauex.tau.ac.il

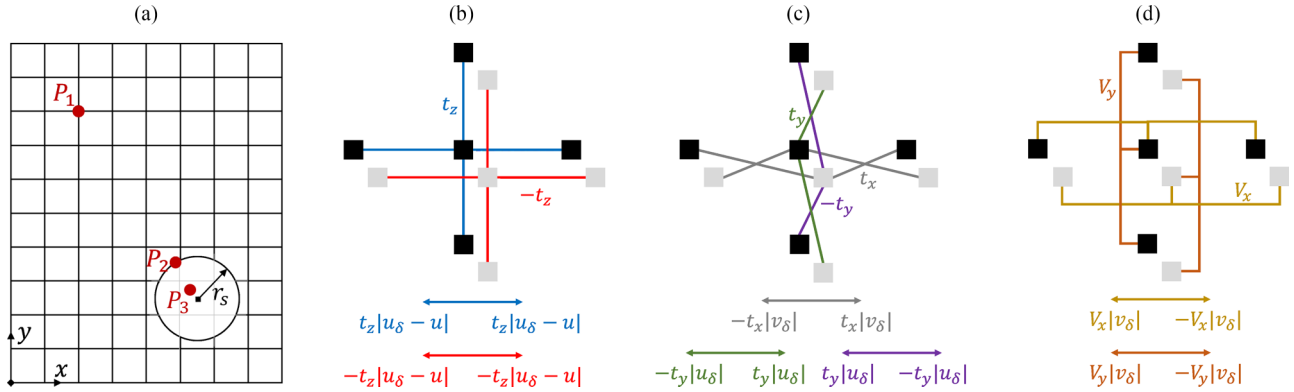

FIG. 1. The mechanical circuit network imitating curved spacetime. (a) The network schematic with a black hole of radius r_s. $P_{1,2,3}$ indicate representative locations outside the hole, on the horizon and inside the hole. (b)–(d) The unit cell with the target closed-loop couplings $+t_z$, $-t_z$, it_x, t_y, $-t_y$, $iV_x(x, y)$, and $iV_y(x, y)$, depicted in separate panels for clarity. Below the panels are plotted the forces that each element exerts on the masses, as implied by the Hamiltonian in Eq. (2). δ indicates the nearest-neighbor mass, u is displacement, and v is velocity.

be visualized as semiclassical tunneling of particles through the event horizon [27,28] by considering the following scenario: A pair of positive and negative energy particles is created either just inside the horizon, where a positive energy particle tunnels outward, or just outside the event horizon, where a negative energy particle tunnels inward. Tunneling of a particle with energy E is compensated by an equivalent mass loss within the black hole for which the emission rate is given by

$$\Gamma_H \approx \exp\left(-\frac{\hbar E}{K_B T_H}\right). \tag{3}$$

Remarkably, Hawking temperature is proportional to the gravitational field strength g as $K_B T_H = \hbar g/2\pi c = \hbar c^3/8\pi GM$, where K_B is the Boltzmann constant, $\hbar$ is the Planck constant, and G stands for the universal gravitational constant. Here, T_H is inversely proportional to the black hole mass M, and for a small black hole (solar mass) currently present in our universe, T_H is of the order of $\approx 10^{-6}$ K [29]. As this value is six orders of magnitude smaller than the cosmic microwave background, it is overshadowed, thus remaining undetected. This motivated a search for event horizon analogues, based on wave propagation in counterflowing fluids and associated ideas in photonics and Bose-Einstein condensates [30–39]. In the proposed mechanical circuit platform, we realize horizon tunneling based on the same WSM formalism as for gravitational lensing, solely by reprogramming the artificial potential in Eq. (2). Our model relies on the mechanical wave packet tunneling through a synthetic horizon, which makes it completely distinct from the pair production mechanism [27,28].

II. GRAVITATIONAL LENSING ANALOGUE

The platform is illustrated in Fig. 1(a). This is a two-dimensional square network with the black hole represented by a circle of radius r_s. This network needs to realize a synthetic curved spacetime, and thus, its dynamical matrix needs to fully retrieve the quantum Hamiltonian in Eq. (2). The unit cell of the network, as depicted in Figs. 1(b)–1(d), consists of masses at two sites, A (black squares) and B (gray squares), with a single degree of freedom per site, e.g., vibrating out-of-plane with a displacement u and velocity v. Following Eq. (2), the masses are directly coupled by t_z (blue bars), $-t_z$ (red bars), $iV_x(x, y)$ (yellow bars), and $iV_y(x, y)$ (orange bars) and are cross-coupled by it_x (gray bars), t_y (green bars), and $-t_y$ (violet bars). For the circle perimeter to represent the horizon, the quantum potential $V_t(r)$, and thus the corresponding couplings in the network, needs to equal v_f (or 1 in a normalized formulation) at the perimeter $r = r_s$ [12,13]. To support the lensing phenomenon, the potential strength also needs to increase toward the circle origin $r = 0$. A specific expression is set at the model validation stage.

The nature of each coupling is illustrated below the panels with the subscript δ indicating the nearest connected mass. The $+t_z$ coupling is reciprocal and stable and can be realized by a linear spring. The $-t_z$ coupling is reciprocal but is inherently unstable due to the negative sign, equivalent to a spring that expands when stretched. The complex-valued couplings it_x, $iV_x(x, y)$, and $iV_y(x, y)$ relate to the mass velocities, as the Fourier transform of $v = \dot{u}$ equals $i\Omega u$. These couplings, as well as $\pm t_y$, lack a restoring force and have an opposite sign at each end, being thus both nonreciprocal and unstable (but the total system is Hermitian).

As all the couplings except $+t_z$ cannot be implemented by passive elements, we implement them in our network using an active feedback mechanism [40–50]. This mechanism is embedded in a stable host network consisting of the $+t_z$ couplings only, shown by the blue bars in the schematic in Figs. 2(a) and 2(b). An active controller generates commands for external forces f^A, f^B at each unit cell, operating in a real-time closed loop. These forces are responsible for creating the couplings $-t_z$, it_x, $\pm t_y$, $iV_x(x, y)$, and $iV_y(x, y)$ as well as to stabilize the overall system. In the $\{m, n\}$ A/B sites, Figs. 2(a) and 2(b), the action of $f^{A/B}$ is based on velocity measurements of the $\{m \pm 1, n\}$ and $\{m, n \pm 1\}$ A/B sites and of the $\{m \pm 1, n\}$ B/A sites, respectively indicated by the yellow, orange, and gray arrows, as well as displacement measurements of the $\{m, n \pm 1\}$ B/A sites, indicated by the green/violet arrows. The action of f^B alone is also based on displacement measurements of the $\{m \pm 1, n\}$ and $\{m, n \pm 1\}$ B sites, indicated by the red arrows. In

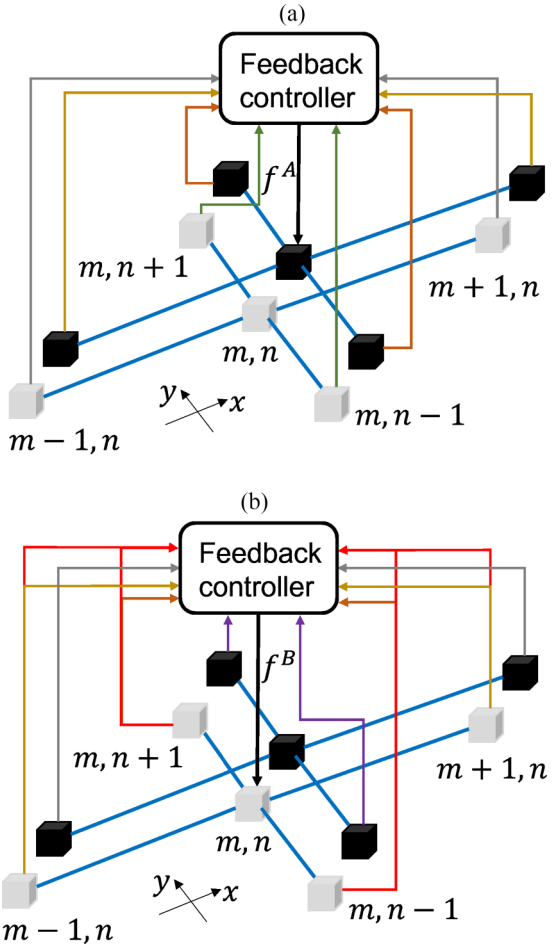

FIG. 2. Control mechanism implementation scheme. (a) and (b) The actuation (black) and measurement (color) signals at the $\{m, n\}$ unit cell for the A and B sites, respectively.

addition, the action of $f^{A/B}$ is based on displacement measurements of $\{m, n\}$ A/B sites (not indicated in the figure). The measured signals are fed back in real time into the electronic controller, the gains of which are programed into the matrix C. The algorithm is given by

$$\begin{bmatrix} f^A \\ f^B \end{bmatrix} = -C \begin{bmatrix} \mathbf{u} \\ \mathbf{v} \end{bmatrix}, \quad C = \frac{1}{2} \begin{bmatrix} C_u^A & C_v^A \\ C_u^B & C_v^B \end{bmatrix},$$
$$\begin{cases} C_u^A = [-\beta \quad 0 \quad 0 \quad 0 \quad -t_y \quad t_y \quad 0 \quad 0] \\ C_u^B = [0 \quad t_y \quad -t_y \quad -(\beta + 8t_z) \quad 2t_z \quad 2t_z \quad 2t_z \quad 2t_z] \\ C_v^A = [V_x \quad -V_x \quad V_y \quad -V_y \quad -t_x \quad t_x \quad 0 \quad 0] \\ C_v^B = [-t_x \quad t_x \quad 0 \quad 0 \quad V_x \quad -V_x \quad V_y \quad -V_y], \end{cases} \tag{4}$$

where $\mathbf{u}^{A/B} = [\ u^{A/B}_{m,n} \quad u^{A/B}_{m,n+1} \quad u^{A/B}_{m,n-1} \quad u^{B}_{m+1,n} \quad u^{B}_{m-1,n}\ ]$ and $\mathbf{v}^{A/B} = [\ v^{A/B}_{m+1,n} \quad v^{A/B}_{m-1,n} \quad v^{A/B}_{m,n+1} \quad v^{A/B}_{m,n-1}\ ]$ constitute the measurement signals $\mathbf{u} = [\ \mathbf{u}^A \quad \mathbf{u}^B\ ]'$ and $\mathbf{v} = [\ \mathbf{v}^A \quad \mathbf{v}^B\ ]'$ for the $\{m, n\}$ unit cell, $V_{x/y} = V_{x/y}(x_{m,n}, y_{m,n})$ is the potential, and $\beta = -8t_z$ guarantees the overall system stability.

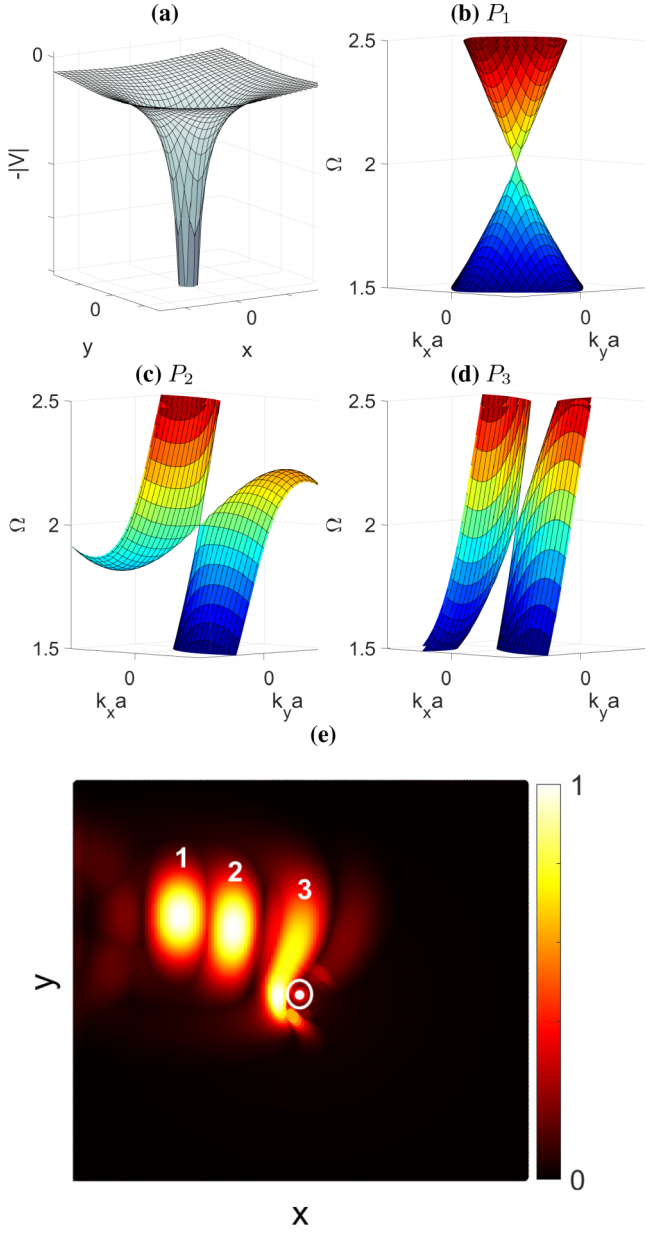

FIG. 3. Synthetic curved spacetime validation in momentum and real space. (a) The potential $V_t(r)$. (b)–(d) The classical frequency spectrum corresponding to outside the hole, on the horizon, and inside the hole locations, indicated by the points P_1, P_2, and P_3 in Fig. 1(a) and respectively evolving from nontilted, critically tilted, and overtilted cones. (e) Time domain wave packet propagation across the network, plotted at increasing time instances (1,2,3) and featuring the expected bending toward the black hole (white circle).

Next, we demonstrate that the closed-loop system resulting from Eq. (4) fully satisfies the properties of curved spacetime, both in momentum and in real space. Due to the velocity terms, in momentum space, we obtain a quadratic eigenvalue problem (see Appendix A for details). The potential is selected in the funnel form $V_t(r) = \gamma/r$, Fig. 3(a), where $\gamma > 0$ is analogous to the black hole mass [12]. The estimation of grid size in Fig. 1(a) is contingent upon the parameter γ. If $V_t(r)$ decays faster while crossing the horizon, the grid size is

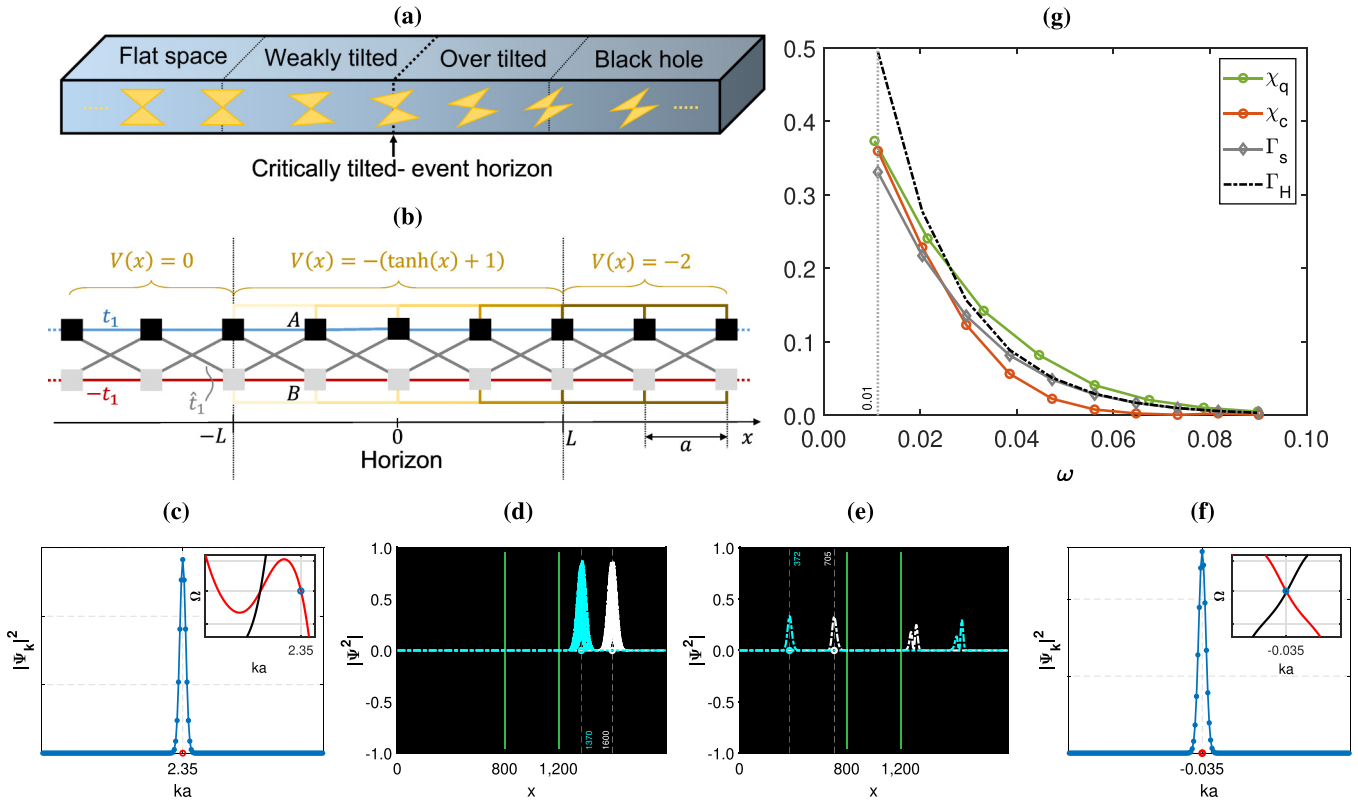

FIG. 4. Artificial Hawking horizon tunneling. (a) Schematic of the Weyl semimetal (WSM) along the principle path. The spatially varying tilt (gold cones) represents the interface between the black hole (overtilted cones) and flat space (zero-tilted cones). The transition occurs at the critical tilt, which represents the event horizon. (b) The relevant portion of the mechanical network of Fig. 1. (c) Fourier transform of the initial wave packet in flat space. (d) and (e) Time evolution of a Gaussian wave packet across the artificial horizon (green lines) of length $N_0 = 400$ and side sizes $N_L, N_R = 800$, tilt rate $\gamma_t = 0.1$, lattice constant $a = 1$, and coupling strength $t_x, t_z = 1$. At time T_0, the wave packet is launched at position $x_0 = 1600$. (d) The response (absolute value) before tunneling at T_0 (white) and $T_1 = 198$ (cyan). (e) The response after tunneling at $T_2 = 1174$ (white) and $T_3 = 1845$ (cyan). (f) Fourier transform of the time domain response at T_3. (g) Variation with ω of the original high-energy emission rate Γ_H (black), the classical equivalence for the analytical quantum transmission probability in the condensed matter formalism Γ_s (gray), the numerically calculated quantum decay rate χ_q (green), and the numerically calculated classical decay rate χ_c (orange) for $\gamma_t = 0.1$.

expected to be smaller than the scenario where $V_t(r)$ decays at a slower rate. In Figs. 3(b)–3(d), we plot the classical frequency spectrum (zoom-in) for three representative locations across the spacetime, which are outside the hole, on the horizon, and inside the hole, as respectively indicated by P_1, P_2, and P_3 on top of the sketch of Fig. 1(a). As expected, outside the hole, the spectrum is nontilted but becomes critically tilted at the horizon and overtilted inside the hole. We then numerically simulate the time domain evolution of a wave packet, as depicted in Fig. 3(e) for three time instances. The wave packet, which is launched far from the black hole (white circle), propagates across the network in a curved trajectory, indicating the expected bending toward the hole center.

III. HAWKING TUNNELING ANALOGUE

To demonstrate the versatility of our network, we reprogram the controller in Eq. (4) to support the horizon tunneling phenomenon. Unlike lensing, for tunneling, a one-dimensional interface of gradually tilted dispersion cones is sufficient, as illustrated in Fig. 4(a). The cones range from zero-tilted to overtilted, respectively standing for flat space and the black hole. The critically tilted cone represents the event horizon. We thus reprogram the controller to switch off the couplings in the y direction, Fig. 4(b), and to generate the potential $V_t(x) = -(1 + \tanh \gamma_t x)$. Here, γ_t determines the rate of change of $V_t(x)$ across the horizon, which is directly mapped to the gravitational field strength g through $\gamma_t = g/c$. This potential defines the interface $-L \leqslant x \leqslant L$ by satisfying $\tanh(L) \approx 1$. Outside the interface, i.e., at $x < -L$ and $x > L$, $V_t(x)$ takes the constant end values 0 and 2, respectively. Here, $x = 0$ is the critical tilt point indicating the artificial event horizon.

We validate the tunneling analogue by launching a Bloch-mode-modulated Gaussian wave packet from the overtilted region of the Fourier transform depicted in Fig. 4(c) and simulating its time evolution as it tunnels through the artificial horizon to the flat space region, as depicted in Figs. 4(d) and 4(e). The Fourier transform of the transmitted wave packet, as predicted by energy conservation, is depicted in Fig. 4(f). Both momenta are indicated by a blue circle on top of the corresponding dispersion band in the insets (see Appendix B for details). Then defining ω as the difference between the initial wave packet frequency and the classical spectrum crossing

point, we rewrite Eq. (3) as $\Gamma_H = \exp(-2\pi E/\gamma_t)$, which is the limit of the analytical quantum transmission probability $\Gamma_s = 1/[1+\exp(2\pi E/\gamma_t)]$ [51,52], and consider the classical equivalence $\omega = E$. We then define the numerical decay rate for the quantum χ_q and the classical χ_c models, with $\Psi_m^{\rm f}$ and $\Psi_m^{\rm in}$ as the squared amplitudes of the final and initial wave packets, obtained from time domain simulations via $\chi_{q/c} = \sum_m^{N_L} |\Psi_m^{\rm f}|^2 / \sum_m^{N_R} |\Psi_m^{\rm in}|^2$. The dependence of Γ_H (black), Γ_s (gray), χ_q (green), and χ_c (orange) on ω is depicted in Fig. 4(g). Remarkably, we observe that, as a function of ω, χ_c closely follows the profile of χ_q, Γ_s, and Γ_H. This validates our system as a classical analogue of Hawking phenomena.

IV. CONCLUSIONS

To conclude, we proposed a purely classical realization of artificial curved spacetime, based on WSM formalism. Our model features a two-dimensional network of mass elements, the collective dynamics of which is equivalent to WSM with inhomogeneous potential and the associated varying dispersion tilt. The resulting mechanical circuits required unstable and nonreciprocal couplings, which were created in real time using embedded active feedback controller. Despite the instability of the individual couplings, the control algorithm managed to stabilize the overall network. The wide operational bandwidth of the feedback loop electrical circuitry, typically at the order of megahertz, ensures that the latency of the mechanical system excitation, typically at the order of Hertz, is negligible.

Our model produced the required space-dependent tilt strength for gravitational analogues in a bulk material, thus offering enhanced experimental freedom compared with electronic WSM [53–55]. Using dynamical simulations, we demonstrated bending of mechanical wave packets toward an artificial black hole in the network center, manifesting the gravitational lensing phenomenon. By reprogramming the controller gains, we mimicked horizon tunneling on the same platform. The attenuation rate of a tunneled wave packet matched well with the transmission probability of the quantum system as well as the emission rate of the original black hole. The reprogrammable nature of our platform enables to test, e.g., the effect of black holes of different sizes on lensing and tunneling, and on other high-energy phenomena related to curved spacetime.

ACKNOWLEDGMENTS

The authors are grateful to Steven Cummer, John Smith, Martin Wegener, Romain Fleury, Badreddine Assouar, Bogdan Popa, Jensen Li, Vincenzo Vitelli, and Chen Shen for insightful discussions. A special thanks goes to Daniel Sabsovich for important comments at the beginning of this project.

APPENDIX A: GRAVITATIONAL LENSING ANALOGUE—DERIVATION DETAILS

Here, we give the derivation details of the synthetic gravitational lensing results in Fig. 3. The open-loop equations of motion for the $\{m,n\}$ unit cell are given by

$$\ddot{u}_{m,n}^{A/B} = \tfrac{1}{2}t_z\big(-4u_{m,n}^{A/B} + u_{m+1,n}^{A/B} + u_{m-1,n}^{A/B} + u_{m,n+1}^{A/B} + u_{m,n-1}^{A/B}\big) + f_{m,n}^{A/B}. \tag{A1}$$

With the control algorithm defined by Eq. (4), the closed-loop classical dynamics, for which the time domain simulation in Fig. 3(e) was carried out, takes the form:

$$\begin{aligned}\ddot{u}_{m,n}^{A/B} = {}& \pm\tfrac{1}{2}t_z\big(-4u_{m,n}^{A/B} + u_{m+1,n}^{A/B} + u_{m-1,n}^{A/B} \\ & + u_{m,n+1}^{A/B} + u_{m,n-1}^{A/B}\big) - 4t_z u_{m,n}^{A/B} \\ & + \tfrac{1}{2}t_x\big(-v_{m+1,n}^{B/A} + v_{m-1,n}^{B/A}\big) \\ & \pm \tfrac{1}{2}t_y\big(-u_{m,n+1}^{B/A} + u_{m,n-1}^{B/A}\big) \\ & + \tfrac{1}{2}V_x\big(-v_{m+1,n}^{A/B} + v_{m-1,n}^{A/B}\big) \\ & + \tfrac{1}{2}V_y\big(-v_{m,n+1}^{A/B} + v_{m,n-1}^{A/B}\big).\end{aligned} \tag{A2}$$

The frequency domain plots of the closed-loop dispersion relation in Figs. 3(a)–3(d) were obtained by substituting the solution $\mathbf{u}_{m,n}^{A/B}(t) = \mathbf{u}_{\mathbf{k}}^{A/B}\exp[i(\Omega t - \mathbf{k}\cdot\mathbf{r})]$ in Eq. (A2), and given by

$$\begin{aligned}&\Omega^2\sigma_0 + ([t_x\sigma_x + V_x\sigma_0]\sin k_x a + V_y\sigma_0 \sin k_y a)\Omega \\ &+ t_y\sigma_y \sin k_y a - t_z(2 - \cos k_x a - \cos k_y a)\sigma_z \\ &- 4t_z\sigma_0 = 0.\end{aligned} \tag{A3}$$

APPENDIX B: HAWKING RADIATION ANALOGUE—DERIVATION DETAILS

Here, we give the derivation details of the synthetic horizon tunneling results in Fig. 4. The relevant portion of the control scheme is depicted in Fig. 5. The dynamical equations of

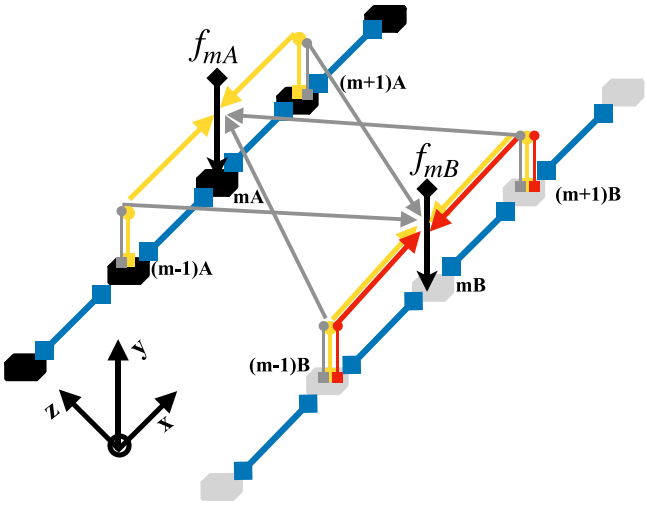

FIG. 5. Control loop details. The host structure features $+t_z$ couplings only and control forces f_{mA} and f_{mB} (black arrows) applied to the masses. The forces are based on the measured velocities $\mathbf{v}_m$ and displacements $\mathbf{u}_m$ at adjacent sites, processed by corresponding controller gains, depicted by red, gray, and yellow arrows, which respectively create the couplings $-t_z$, it_x, and $iV_t(x)$ in real time.

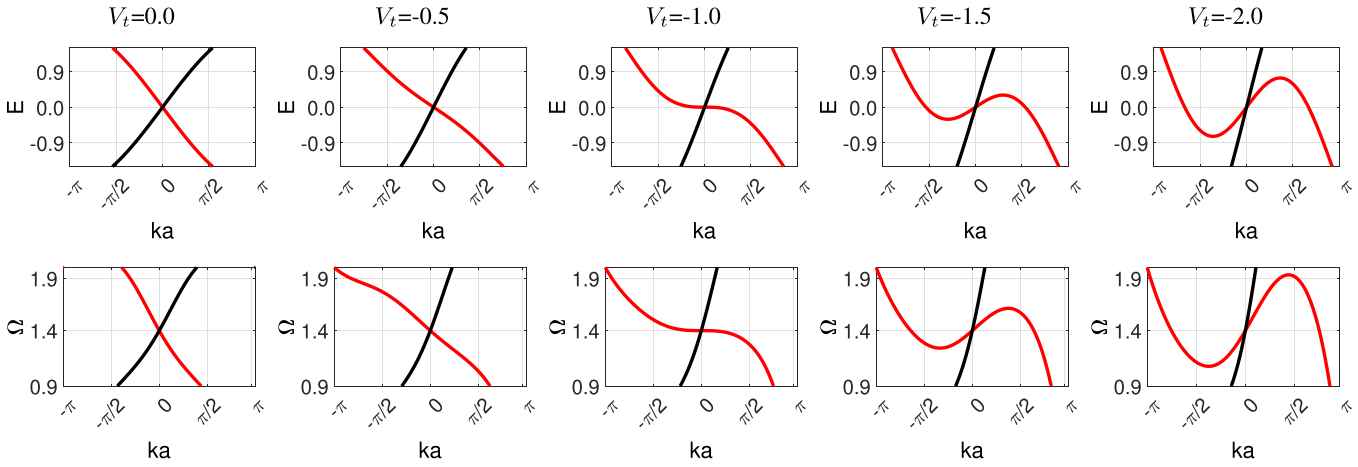

FIG. 6. Top: Energy dispersion of the quantum Weyl semimetal (WSM) Hamiltonian in Eq. (2) along the horizon as a function of tilt strength. Bottom: The corresponding classical frequency dispersion obtained from Eq. (B5).

motion at the unit cell in the open loop read

$$\ddot{u}_m^{A/B} = \tfrac{1}{2}t_z\left(-2u_m^{A/B} + u_{m+1}^{A/B} + u_{m-1}^{A/B}\right) + f_m^{A/B}. \tag{B1}$$

The control law is defined by

$$\begin{pmatrix} f_m^A \\ f_m^B \end{pmatrix} = -C\begin{pmatrix} \mathbf{u}_m \\ \mathbf{v}_m \end{pmatrix}, \tag{B2}$$

with measured displacement $\mathbf{u}_m = (\ u_m^A \quad u_{m-1}^B \quad u_m^B \quad u_{m+1}^B\ )'$ and velocity $\mathbf{v}_m = (\ v_{m+1}^A \quad v_{m-1}^A \quad v_{m+1}^B \quad v_{m-1}^B\ )'$ signals, and the controller matrix

$$C = \frac{1}{2}\begin{bmatrix} 2\beta & 0 \\ 0 & 2t_z \\ 0 & 2(\beta + 2t_z) \\ 0 & 2t_z \\ V_t(x_m) & \hat{t}_z \\ -V_t(x_m) & -\hat{t}_z \\ \hat{t}_z & V_t(x_m) \\ -\hat{t}_z & -V_t(x_m) \end{bmatrix}', \tag{B3}$$

where $\beta = 2t_z$. The closed-loop classical dynamics, for which the time domain simulation of Figs. 4(c) and 4(d) was obtained, takes the form:

$$\begin{aligned} \ddot{u}_m^{A/B} = {} & \pm\tfrac{1}{2}t_z\left(-2u_m^{A/B} + u_{m+1}^{A/B} + u_{m-1}^{A/B}\right) - \beta u_m^{A/B} \\ & + \tfrac{1}{2}t_x\left(-v_{m+1}^{A/B} + v_{m-1}^{A/B}\right) \\ & + \tfrac{1}{2}V_t(x_m)\left(-v_{m+1}^{B/A} + v_{m-1}^{B/A}\right). \end{aligned} \tag{B4}$$

Now we give the derivation details of the spectrum equivalence between the quantum and the classical horizon tunneling models, with the latter appearing in the inset of Figs. 4(e) and 4(f) for $V_t = 0$ and $V_t = -2$, respectively. Substituting a plane wave of frequency Ω for the displacement in the closed-loop system in Eq. (B4), $u_m^{A/B}(t) = u_k^{A/B}\exp[i(\Omega t - kx)]$, we obtain the quadratic eigenvalue problem:

$$\begin{aligned} & \Omega^2\sigma_0 + [t_x\sigma_x + V_t\sigma_0]\sin ka\Omega - t_z(1-\cos ka)\sigma_z \\ & \quad - 2t_z\sigma_0 = 0. \end{aligned} \tag{B5}$$

The solution of Eq. (B5) gives the frequency spectrum of our classical mechanical model, which we compare in Fig. 6 with the corresponding energy spectrum of the quantum Hamiltonian in Eq. (2). Both spectra are plotted for the entire range of the interface, from zero-tilt $V_t = 0$ to the overtilt $V_t = -2$, through the critical tilt $V_t = -1$. In the classical spectrum, the stability correction β introduced by our control algorithm shifts the crossing point to a finite positive frequency. Remarkably, despite the profound difference between the quantum first-order and the classical second-order dynamics, the shape of both dispersion curves evolves in a similar way from a linear and near-even dispersion at the zero tilt to the nonlinear and near-odd dispersion at the overtilt.

The details of the tunneling rate validation, depicted by the orange curve ξ_c in Fig. 4(g) are given next. We excite the initial displacements and velocities of the masses with the Gaussian wave packet:

$$\Psi_m = \cos(k_i x_m)\exp\left[\frac{(x-x_i)^2}{4\delta^2}\right]\phi_{k_i}^{\alpha}, \tag{B6}$$

in the overtilted region $V_t = -2$. The system hosts a two-band model with $\alpha = 1, 2$ shown respectively by red and black in Fig. 6, and $\phi_{k_i}^{\alpha}$ represents the eigenvector associated with the frequency band Ω_α. The product of the eigenvector with the initial Gaussian envelope captures the required initial state at momentum k_i. The initial wave packet velocity in the out-of-plane direction is determined by the time derivative of the displacement $\dot{\Psi}_m$ to ensure unidirectional propagation through the interface.

Here, we detail the calculation of Fourier transformation, which describes the momentum space distribution of the real-space wave packet Ψ_m, depicted in Figs. 4(e) and 4(f), and the corresponding group velocity calculation. The Fourier

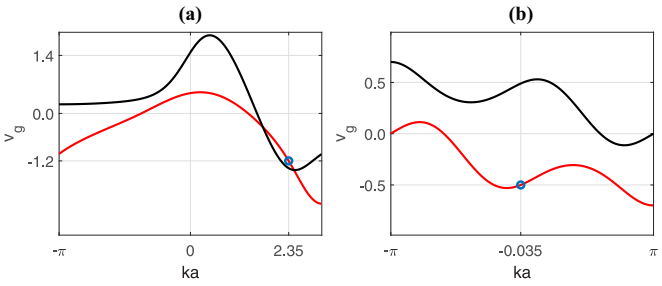

FIG. 7. Group velocity calculation (black, red curves) obtained analytically from the dispersion diagrams of the (a) $V_t = -2$ and (b) $V_t = 0$ regions, and numerically (blue dots) from the time domain simulations in these regions, respectively given by $v_g = -230/198 \approx -1.2$ and $v_g = -333/671 \approx -0.5$ units, coinciding with the predicted value.

transformation is defined as

$$\Psi_{k_l} = \frac{1}{\sqrt{N}} \sum_m \exp(ik_l x_m)\Psi_m, \tag{B7}$$

where N is the total system size. The group velocity is calculated using $v_g = d\omega/dk$. In Figs. 7(a) and 7(b), we show the variation of v_g for both the frequency band in the $V_t = -2$ and $V_t = 0$ regions. For a particular eigenfrequency $\omega = 1.4274$, respective group velocities in both the $V_t = -2$ and $V_t = 0$ regions are pointed by the blue circles.

Finally, we present the dynamical simulation details of the quantum WSM system χ_q, plotted by the green curve in Fig. 4(g). An initial quantum wave packet Ψ^q_{in} is created in the $V_t = -2$ region at position x_0 with momentum k_i:

$$\Psi^q_m = \exp(ik_i x_m) \exp\left[\frac{(x - x_i)^2}{4\delta^2}\right] \phi^\alpha_{k_i}, \tag{B8}$$

where $\phi^\alpha_{k_i}$ represents the eigenvector associated with the energy band E_α. The time evolution of the wave packet is governed by solving the Schrödinger equation:

$$i\hbar\partial_t \Psi^q(t) = H\Psi^q(t), \tag{B9}$$

where the Hamiltonian H includes all the real and imaginary valued couplings in real space obtained from Eq. (2). Equation (B9) is then numerically solved using state space formulation, producing the green curve χ_q.

One can also calculate the final wave packet at time t by using the analytical solution of Eq. (B9), given as

$$\Psi^q(t) = \sum_\nu |\nu\rangle \langle\nu|\Psi^q(t = 0)\rangle \exp\left(-\frac{i\epsilon_\nu t}{\hbar}\right), \tag{B10}$$

where $|\nu\rangle$ represents the νth eigenvector of the Hamiltonian H with associated eigenenergy, and the initial condition $\langle\nu|\Psi^q(t = 0)\rangle = \sum_j [c^\nu_j]^* \Psi^q_j$. Here, c^ν_j represents the conjugate of jth component of the νth eigenvector. Solving for the final position (site) of the wave packet at time t reads

$$\begin{aligned}\Psi^q_m(t) &= \sum_\nu \langle m|\nu\rangle \sum_j \left[c^\nu_j\right]^* \Psi^q_j \exp\left(-\frac{i\epsilon_\nu t}{\hbar}\right) \\ &= \sum_\nu c^\nu_m \sum_j \left[c^\nu_j\right]^* \Psi^q_j \exp\left(-\frac{i\epsilon_\nu t}{\hbar}\right).\end{aligned} \tag{B11}$$

[1] V. P. Frolov and A. Zelnikov, *Introduction to Black Hole Physics* (Oxford University Press, Oxford, 2011).

[2] C. W. Misner, K. S. Thorne, and J. A. Wheeler, *Gravitation* (WH Freeman and Co, San Francisco 1973).

[3] G. E. Volovik, Black hole and Hawking radiation by type-II Weyl fermions, JETP Lett. **104**, 645 (2016).

[4] M. A. Zubkov, The black hole interior and the type II Weyl fermions, Mod. Phys. Lett. A **33**, 1850047 (2018).

[5] H. Huang, K.-H. Jin, and F. Liu, Black-hole horizon in the Dirac semimetal $Zn_2In_2S_5$, Phys. Rev. B **98**, 121110(R) (2018).

[6] L. Liang and T. Ojanen, Curved spacetime theory of inhomogeneous Weyl materials, Phys. Rev. Res. **1**, 032006(R) (2019).

[7] Y. Kedem, E. J. Bergholtz, and F. Wilczek, Black and white holes at material junctions, Phys. Rev. Res. **2**, 043285 (2020).

[8] V. Könye, C. Morice, D. Chernyavsky, A. G. Moghaddam, J. van den Brink, and J. van Wezel, Horizon physics of quasi-one-dimensional tilted Weyl cones on a lattice, Phys. Rev. Res. **4**, 033237 (2022).

[9] P. Painlevé, Classical mechanics and the theory of relativity, Astronomy **36**, 6 (1922).

[10] A. Gullstrand, *General Solution of the Static One-Body Problem in Einstein's Theory of Gravitation* (Almqvist & Wiksell, Stockholm, 1922).

[11] G. Lemaître, L'Univers en expansion, *Annales de la Société Scientifique de Bruxelles* (1933), Vol. 53, p. 51 .

[12] V. Könye, L. Mertens, C. Morice, D. Chernyavsky, A. G. Moghaddam, J. van Wezel, and J. van den Brink, Anisotropic optics and gravitational lensing of tilted Weyl fermions, Phys. Rev. B **107**, L201406 (2023).

[13] A. Haller, S. Hegde, C. Xu, C. De Beule, T. L. Schmidt, and T. Meng, Black hole mirages: Electron lensing and Berry curvature effects in inhomogeneously tilted Weyl semimetals, SciPost Phys. **14**, 119 (2023).

[14] M. I. Katsnelson, K. S. Novoselov, and A. K. Geim, Chiral tunnelling and the Klein paradox in graphene, Nat. Phys. **2**, 620 (2006).

[15] J. Behrends, S. Roy, M. H. Kolodrubetz, J. H. Bardarson, and A. G. Grushin, Landau levels, Bardeen polynomials, and Fermi arcs in Weyl semimetals: Lattice-based approach to the chiral anomaly, Phys. Rev. B **99**, 140201(R) (2019).

[16] X. Jiang, C. Shi, Z. Li, S. Wang, Y. Wang, S. Yang, S. G. Louie, and X. Zhang, Direct observation of Klein tunneling in phononic crystals, Science **370**, 1447 (2020).

[17] L. Sirota, Klein-Like Tunneling of Sound via Negative Index Metamaterials, Phys. Rev. Appl. **18**, 014057 (2022).

[18] R. Süsstrunk and S. D. Huber, Observation of phononic helical edge states in a mechanical topological insulator, Science **349**, 47 (2015).

[19] L. M. Nash, D. Kleckner, A. Read, V. Vitelli, A. M. Turner, and W. T. M. Irvine, Topological mechanics of gyroscopic metamaterials, Proc. Natl. Acad. Sci. USA **112**, 14495 (2015).

[20] S. H. Mousavi, A. B. Khanikaev, and Z. Wang, Topologically protected elastic waves in phononic metamaterials, Nat. Commun. **6**, 8682 (2015).

[21] R. K. Pal and M. Ruzzene, Edge waves in plates with resonators: An elastic analogue of the quantum valley Hall effect, New J. Phys. **19**, 025001 (2017).
[22] R. Chaunsali, C.-W. Chen, and J. Yang, Subwavelength and directional control of flexural waves in zone-folding induced topological plates, Phys. Rev. B **97**, 054307 (2018).
[23] Y. Zhou, P. R. Bandaru, and D. F. Sievenpiper, Quantum-spin-Hall topological insulator in a spring-mass system, New J. Phys. **20**, 123011 (2018).
[24] S. W. Hawking, Black hole explosions? Nature (London) **248**, 30 (1974).
[25] S. W. Hawking, Particle creation by black holes, in *Euclidean Quantum Gravity* (World Scientific, Singapore, 1975), pp. 167–188.
[26] J. D. Bekenstein, Black holes and entropy, Phys. Rev. D **7**, 2333 (1973).
[27] K. Srinivasan and T. Padmanabhan, Particle production and complex path analysis, Phys. Rev. D **60**, 024007 (1999).
[28] M. K. Parikh and F. Wilczek, Hawking Radiation As Tunneling, Phys. Rev. Lett. **85**, 5042 (2000).
[29] S. J. Robertson, The theory of Hawking radiation in laboratory analogues, J. Phys. B: At., Mol. Opt. Phys. **45**, 163001 (2012).
[30] W. G. Unruh, Experimental Black-Hole Evaporation? Phys. Rev. Lett. **46**, 1351 (1981).
[31] L. J. Garay, J. R. Anglin, J. I. Cirac, and P. Zoller, Sonic Analog of Gravitational Black Holes in Bose-Einstein Condensates, Phys. Rev. Lett. **85**, 4643 (2000).
[32] U. Leonhardt and P. Piwnicki, Relativistic Effects of Light in Moving Media with Extremely Low Group Velocity, Phys. Rev. Lett. **84**, 822 (2000).
[33] U. Leonhardt, A laboratory analogue of the event horizon using slow light in an atomic medium, Nature (London) **415**, 406 (2002).
[34] S. Giovanazzi, Hawking Radiation in Sonic Black Holes, Phys. Rev. Lett. **94**, 061302 (2005).
[35] R. Schützhold and W. G. Unruh, Hawking Radiation in an Electromagnetic Waveguide? Phys. Rev. Lett. **95**, 031301 (2005).
[36] S. Weinfurtner, E. W. Tedford, M. C. Penrice, W. G. Unruh, and G. A. Lawrence, Measurement of Stimulated Hawking Emission in an Analogue System, Phys. Rev. Lett. **106**, 021302 (2011).
[37] J. Hu, L. Feng, Z. Zhang, and C. Chin, Quantum simulation of Unruh radiation, Nat. Phys. **15**, 785 (2019).
[38] J. Carot and B. O. J. Tupper, Spherically symmetric magnetohydrodynamics in general relativity, Phys. Rev. D **59**, 124017 (1999).
[39] M. Tajik, M. Gluza, N. Sebe, P. Schüttelkopf, F. Cataldini, J. Sabino, F. Møller, S.-C. Ji, S. Erne, G. Guarnieri *et al.*, Experimental observation of curved light-cones in a quantum field simulator, Proc. Natl. Acad. Sci. USA **120**, e2301287120 (2023).
[40] T. Hofmann, T. Helbig, C. H. Lee, M. Greiter, and R. Thomale, Chiral Voltage Propagation and Calibration in a Topolectrical Chern Circuit, Phys. Rev. Lett. **122**, 247702 (2019).
[41] M. Brandenbourger, X. Locsin, E. Lerner, and C. Coulais, Non-reciprocal robotic metamaterials, Nat. Commun. **10**, 4608 (2019).
[42] L. Sirota, F. Semperlotti, and A. M. Annaswamy, Tunable and reconfigurable mechanical transmission-line metamaterials via direct active feedback control, Mech. Syst. Signal Process. **123**, 117 (2019).
[43] A. Darabi, M. ColLet, and M. J. Leamy, Experimental realization of a reconfigurable electroacoustic topological insulator, Proc. Natl. Acad. Sci. USA **117**, 16138 (2020).
[44] C. Scheibner, W. T. M. Irvine, and V. Vitelli, Non-Hermitian Band Topology and Skin Modes in Active Elastic Media, Phys. Rev. Lett. **125**, 118001 (2020).
[45] M. I. N. Rosa and M. Ruzzene, Dynamics and topology of non-Hermitian elastic lattices with non-local feedback control interactions, New J. Phys. **22**, 053004 (2020).
[46] T. Helbig, T. Hofmann, S. Imhof, M. Abdelghany, T. Kiessling, L. W. Molenkamp, C. H. Lee, A. Szameit, M. Greiter, and R. Thomale, Generalized bulk-boundary correspondence in non-Hermitian topolectrical circuits, Nat. Phys. **16**, 747 (2020).
[47] L. Sirota, R. Ilan, Y. Shokef, and Y. Lahini, Non-Newtonian Topological Mechanical Metamaterials Using Feedback Control, Phys. Rev. Lett. **125**, 256802 (2020).
[48] L. Sirota, D. Sabsovich, Y. Lahini, R. Ilan, and Y. Shokef, Real-time steering of curved sound beams in a feedback-based topological acoustic metamaterial, Mech. Syst. Signal Process. **153**, 107479 (2021).
[49] O. Lasri and L. Sirota, Active control approach to temporal acoustic cloaking, Appl. Phys. Lett. **123**, 032201 (2023).
[50] L. Zhang, Y. Yang, Y. Ge, Y.-J. Guan, Q. Chen, Q. Yan, F. Chen, R. Xi, Y. Li, D. Jia *et al.*, Acoustic non-Hermitian skin effect from twisted winding topology, Nat. Commun. **12**, 6297 (2021).
[51] C. De Beule, S. Groenendijk, T. Meng, and T. Schmidt, Artificial event horizons in Weyl semimetal heterostructures and their non-equilibrium signatures, SciPost Phys. **11**, 095 (2021).
[52] D. Sabsovich, P. Wunderlich, V. Fleurov, D. I. Pikulin, R. Ilan, and T. Meng, Hawking fragmentation and Hawking attenuation in Weyl semimetals, Phys. Rev. Res. **4**, 013055 (2022).
[53] H. F. Yang, L. X. Yang, Z. K. Liu, Y. Sun, C. Chen, H. Peng, M. Schmidt, D. Prabhakaran, B. A. Bernevig, C. Felser *et al.*, Topological Lifshitz transitions and Fermi arc manipulation in Weyl semimetal NbAs, Nat. Commun. **10**, 3478 (2019).
[54] K. Deng, G. Wan, P. Deng, K. Zhang, S. Ding, E. Wang, M. Yan, H. Huang, H. Zhang, Z. Xu *et al.*, Experimental observation of topological Fermi arcs in type-II Weyl semimetal $MoTe_2$, Nat. Phys. **12**, 1105 (2016).
[55] P. Li, Y. Wen, X. He, Q. Zhang, C. Xia, Z.-M. Yu, S. A. Yang, Z. Zhu, H. N. Alshareef, and X.-X. Zhang, Evidence for topological type-II Weyl semimetal WTe_2, Nat. Commun. **8**, 2150 (2017).